Inorganic Chemistry

Article

pubs.acs.org/IC

Relationship between Spin Ordering, Entropy, and Anomalous Lattice Variation in $Mn_3Sn_{1-\varepsilon}Si_\varepsilon C_{1-\delta}$ Compounds

Jun Yan,[†,‡,§] Ying Sun,[†] Yongchun Wen,[†] Lihua Chu,[†] Meimei Wu,[⊥] Qingzhen Huang,*[,‡] Cong Wang,*[,†] Jeffrey W. Lynn,[‡] and Yunlin Chen[§]

[†]Center for Condensed Matter and Materials Physics, Department of Physics, Beihang University, Beijing 100191, China

[‡]NIST Center for Neutron Research, NIST, Gaithersburg, Maryland 20899-6102, United States

[§]School of Science, Beijing Jiaotong University, Beijing 100044, China

[⊥]Department of Nuclear Physics, Chinese Institute of Atomic Energy, Beijing 102413, China

ABSTRACT: The crystal and magnetic structures of antiperovskite compounds Mn_3SnC, $Mn_3Sn_{0.95}C_{0.9}$, and $Mn_3Sn_{0.93}Si_{0.07}C_{0.94}$ were studied as a function of temperature and magnetic field by neutron powder diffraction. For Mn_3SnC, the magnetic field induces a dramatic variation of antiferromagnetic moment and lattice parameter. Because of this spin−lattice coupling, the "square" antiferromagnetic (AFM) structure plays a key role in inducing a negative thermal expansion in the material. Moreover, the thermal expansion parameter is closely related to the rate of change of the AFM moment, which can be controlled by introducing vacancies or by doping. The variations of the AFM moment and lattice parameter in Mn_3SnC with magnetic field make it possible to use the tunable properties for technical applications.

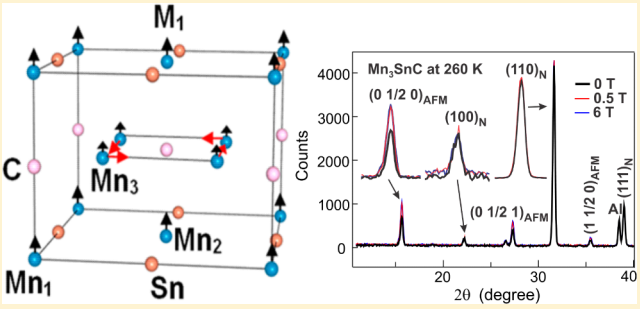

INTRODUCTION

Recently many fascinating physical properties have been found in the antiperovskite compounds, such as superconductivity,[1,2] magnetoresistance,[3−5] and the nearly zero temperature coefficient of resistivity (NZ-TCR).[6−10] Some of these properties are closely associated with their magnetic structure. For example, the negative thermal expansion (NTE) behavior of Ge-doped Mn_3AN (A = Cu, Zn, Ga) is closely related to its antiferromagnetic structure,[11−13] which is different from other types of NTE materials, such as $PbTiO_3$-based compounds[14] or $NaZn_{13}$-type $La(Fe, Si, Co)_{13}$ compounds.[15] The large magnetic entropy change of Mn_3GaC originates from the transition from antiferromagnetic (AFM) to ferromagnetic (FM) under magnetic field.[16−19] Wang et al.[20] reported that Mn_3SnC had a magnetic entropy change of $-\Delta S_m$ = 133 mJ/cm^3 K (corresponding to 17 J/kg K) under a magnetic field of 4.8 T.[20] According to the results of neutron diffraction, the magnetic ground state of Mn_3SnC is a ferrimagnetic (FIM) state.[21] The detailed relationship between the magnetic structure and these properties is still not clear in Mn_3SnC.

In Mn_3CuN, which has the same magnetic structure as Mn_3SnC, the magnetic structure can be changed from the superlattice magnetic structure (propagation vector k = (1/2 1/2 0))[21] to the Γ^{5g}-type antiferromagnetic structure (k = (0 0 0)).[22−24] References 22−24 present the local lattice distortion and the Γ^{5g}-type antiferromagnetic structure in $Mn_3Cu_{1-x}Ge_xN$ as key factors that trigger the large NTE.[22−24] In addition, it has been inferred that the Mn site occupancy affects the rate of the magnetic ordering with temperature, which controls the amount and rate of NTE with temperature in $Mn_{3-x}Cu_{0.5}Ge_{0.5}N$.[25] The effect of vacancies and doping on the magnetic structure and their transitions has also been found in Mn_3Zn_xN, which induced the change from NTE to zero thermal expansion (ZTE) behavior around the magnetic transition. Moreover, the NTE effect could be tuned by the size of the ordered moment in Mn_3ZnN.[26]

Mn_3SnC has the same magnetic structure as Mn_3CuN.[21] However, Mn_3SnC shows a sharp abnormal thermal expansion around the magnetic transition temperature, whereas Mn_3CuN exhibits normal thermal expansion behavior.[21,27] In addition, the NTE effect gradually disappeared with increasing content of Ge in $Mn_3Sn_{1-x}Ge_xC$.[28] It is contrary to the result in Mn_3CuN.

To clarify this discrepancy, we investigated the relation between the magnetic structure and lattice in Mn_3SnC. We studied the evolutions of the lattice and magnetic structure driven by the temperature or the magnetic field. The magnetic structure and negative thermal expansion behavior could be tuned by doping and introducing vacancies. Herein, the relation between the magnetic structure and lattice of $Mn_3Sn_{1-\varepsilon}Si_\varepsilon C_{1-\delta}$ will be discussed in detail.

Received: December 13, 2013
Published: February 3, 2014

   dx.doi.org/10.1021/ic403063t | *Inorg. Chem.* 2014, 53, 2317−2324

EXPERIMENTAL SECTION

Polycrystalline samples with nominal compositions of Mn_3SnC, $Mn_3SnC_{1.1}$, and $MnSn_{0.8}Si_{02}C$ were prepared by a solid-state reaction in vacuum (10^{-5} Pa) using Mn, Sn, and Si with purity of 99.95% and spectroscopic grade carbon powders as starting materials. These materials were mixed in stoichiometric proportion and pressed into pellets. The pellets were wrapped in a tantalum foil, sealed in vacuum in a quartz tube, sintered at 800 K for 100 h, and then cooled to room temperature. The procedure was repeated until a pure single phase was obtained.

Neutron powder diffraction (NPD) data were collected using the BT-1 high-resolution neutron powder diffractometer at NIST Center for Neutron Research (NCNR). A Cu (311) monochromator was used to produce monochromatic neutron beam with wavelength of 1.5403 Å. Neutron diffraction data were collected at various temperatures of interest in the range of 4−300 K to determine the crystal and magnetic structures by Rietveld refinement using the GSAS program,[29] to elucidate the magnetic transitions and thermal expansion properties. The neutron scattering lengths used in the refinement were −0.375, 0.623, 0.665, and 0.415 ($\times 10^{-12}$ cm) for Mn, Sn, C, and Si, respectively.

The NPD patterns at room temperature could be fit well with a structure model of cubic symmetry which has space group $Pm\bar{3}m$ (No. 211) and the following atomic positions: Mn, 3*c* (1/2, 1/2, 0); Sn/Si, 1*a* (0 0 0); and C, 1*b* (1/2,1/2,1/2). The site occupancies of the atoms Mn, Sn, and C were investigated in detail, and the refinement results indicated that the real compositions of the polycrystalline samples Mn_3SnC, $Mn_3SnC_{1.1}$, and $MnSn_{0.8}Si_{02}C$ are often deficient in the cubic corners and body-centered sites. The refined compositions were determined to be $Mn_3Sn_{0.95(1)}C_{0.9(1)}$, $Mn_3SnC_{1.00(1)}$ and $Mn_3Sn_{0.93(4)}Si_{0.07(4)}C_{0.94(1)}$, respectively, and subsequently in this article we will use these refined compositions unless explicitly indicated otherwise. A small amount of MnO, along with other impurities that could not be identified, was found in the $Mn_3Sn_{0.95}C_{0.9}$ and $Mn_3Sn_{0.93}Si_{0.07}C_{0.94}$ samples.

For Mn_3SnC, to clarify the relationship between the entropy change and structure, we also measured the total entropy change during the phase transition, the magnetic entropy change, and the NPD data under magnetic field. To eliminate preferred orientation of powder sample under magnetic field, we pressed the powder into pellets again. According to the NPD data under magnetic field, we did not find any preferred orientation of Mn_3SnC. A differential scanning calorimeter (DSC) was used to measure the crystal and/or magnetic phase transformation and to calculate the transition entropy change of Mn_3SnC. The temperature dependence of the magnetization was measured between 10 and 350 K under magnetic field of 0.01 T using a superconducting quantum interference device (SQUID) magnetometer. The measurement was conducted under field cooling conditions. A set of magnetization isotherms $\mathbf{M}(H)$ at selected temperatures near the phase transition temperature was measured, and the magnetic entropy change was calculated using the Maxwell equation.

RESULTS AND DISCUSSION

First, we analyze the crystal and magnetic structure of Mn_3SnC. Figure 1a shows the crystal structure of Mn_3SnC. The cubic lattice constant of Mn_3SnC is 3.99379 Å at 300 K. The Rietveld refinements were conducted based on the $Pm\bar{3}m$ model. The refinement results of nominal composition $Mn_3SnC_{1.1}$ indicate

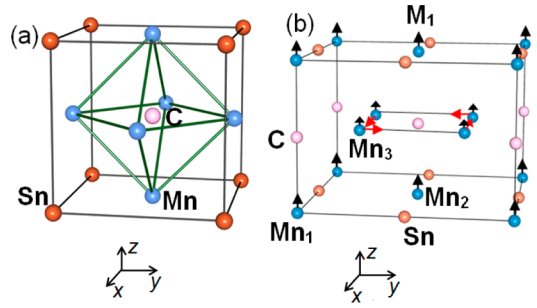

Figure 1. (a) Crystal structure of Mn_3SnC, space group $Pm\bar{3}m$ (No. 211), atomic positions Mn: 3*c*, Sn/Si: 1*a*, C: 1*b*. (b) Magnetic structure ($\sqrt{2}a$, $\sqrt{2}a$, a) model for Mn_3SnC, space group *P*4. We label this magnetic structure model $\mathbf{M}_1$.

that all the crystallography sites were nearly fully occupied; therefore, the corresponding formula is Mn_3SnC. Figure 1b shows the magnetic structure of Mn_3SnC, consistent with that reported in reference 21. The propagation vector k = (1/2 1/2 0) corresponds to an anisotropic magnetic model. The parameters of the magnetic model along the *x*, *y*, and *z* axes are $a_M = \sqrt{2}a$, $b_M = \sqrt{2}a$, $c_M = a$ (a is the lattice parameter of the nuclear structure, a_M, b_M, and c_M are magnetic cell parameters), respectively. The Mn atoms of the superlattice magnetic model are located at three different types of sites of the *P*4 space group: Mn_1 1*a* (0 0 0), Mn_2 1*b* (0.5 0.5 0) and Mn_3 4*d* (0.25 0.25 0.5). Arrows indicate the ordered Mn moment components at these sites. We label the magnetic model $\mathbf{M}_1$. In this model moments for the Mn_3 atoms at the z = 0.5 plane have components with a "square" antiferromagnetic arrangement in the plane and ferromagnetic components in the c_M direction perpendicular to the plane, that is, forming a canted antiferromagnetic arrangement. The moments for the Mn_1 and Mn_2 atoms on the z = 0 plane have only a ferromagnetic component in the c_M direction. This model was used to refine the magnetic structure for data collected at different temperature.

Figure 2a,b shows the neutron powder diffraction data and the Rietveld refinement results for Mn_3SnC at 300K and 15 K, respectively. The diffraction peaks from the Al sample holder were excluded in the analysis. At 300 K, the paramagnetic (PM) state with cubic structure is refined. There are some magnetic peaks appearing at 15 K, as shown in Figure 2b. We fit these magnetic reflections using the superlattice magnetic model $\mathbf{M}_1$. The refined antiferromagnetic moment is 2.69(3) μ_B and the ferromagnetic components are 0.29(22) μ_B for Mn_3, and a ferromagnetic moment 0.9(2) μ_B for Mn_1 and Mn_2 at 15 K. To identify the ferromagnetic peaks, we plot the difference between observed and calculated intensities ($I_{obs} - I_{calc}$) fit by the nuclear-only structure (bottom solid line) and the difference fit by the combined magnetic and nuclear structures (top solid line) in Figure 2c. Comparing the top line with the bottom line in Figure 2c, the magnetic peaks are identified in the bottom line. On the basis of these results, the ferromagnetic peak (1/2 1/2 0) at the nuclear (100) peak position was confirmed.

Figure 3a displays the temperature dependence of the magnetization and inverse susceptibility of Mn_3SnC. The onset temperature of the transition (T_c) from the paramagnetic to the ordered ferrimagnetic state is 283 K. The $1/\chi(T)$ curve labeled by the right axis of Figure 3a indicates the FIM characteristics of Mn_3SnC. Furthermore, we measured the magnetization

dx.doi.org/10.1021/ic403063t | Inorg. Chem. 2014, 53, 2317−2324

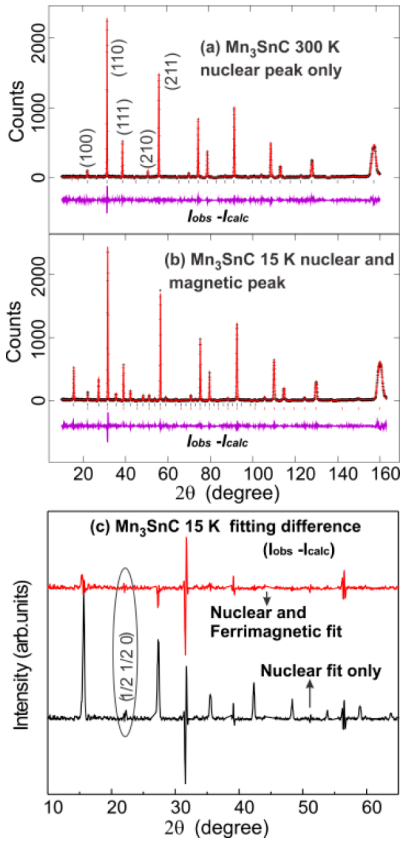

Figure 2. Neutron powder diffraction patterns of Mn_3SnC. (a) Nuclear peak fits at 300 K. (b) Nuclear and magnetic peaks fit at 15 K. The crosses represent the experimental intensities (I_{obs}), the upper solid line represents the calculated intensities (I_{calc}), and the lower solid line is the difference between observed and calculated intensities ($I_{obs} - I_{calc}$). The vertical bars mark the angular positions of the nuclear and magnetic Bragg peaks. (c) The top solid line shows the difference ($I_{obs} - I_{calc}$) generated by nuclear and magnetic fitting with model $\mathbf{M}_1$ at 15 K. The bottom solid line shows the difference ($I_{obs} - I_{calc}$) generated by the nuclear fitting only at 15 K, so that the magnetic contributions are clearly visible.

isotherms of the sample and then calculated the magnetic entropy change by using the Maxwell relation.[30] As shown in Figure 3b, the maximum value of $-\Delta S_M$ is 11.42 J/kg K under an applied field of 5 T. There is also an abnormal lattice contraction of Mn_3SnC near T_c, so that the lattice entropy change will also contribute to the total entropy change. The total entropy changes (ΔS) can be estimated using eq 1:

$$\Delta S = S_{T_2} - S_{T_1} = \int_{T_1}^{T_2} \frac{C_p}{T} dT = \int_{T_1}^{T_2} \frac{dH}{dt}\frac{dt}{dT}\frac{1}{T} dT \quad (1)$$

where C_p, T, H, t, and dH/dt denote the heat capacity at constant pressure, temperature, enthalpy, time, and heat flow, respectively. As shown in Figure 4, the entropy changes (ΔS_{max}) obtained for this transition are −39.8 J/kg K (exothermic process) and 38.5 J/kg K (endothermic process) on cooling and warming, respectively. This result reveals that the magnetic entropy is much smaller than the total entropy.

Usually the magnetic entropy comes from the variation of the ferromagnetic component. However, for Mn_3SnC, the ferromagnetic peak disappeared at 260 K. To pursue the origin of the large magnetic entropy change, we tried to induce the ferromagnetic state by applying magnetic field at 260 and 277

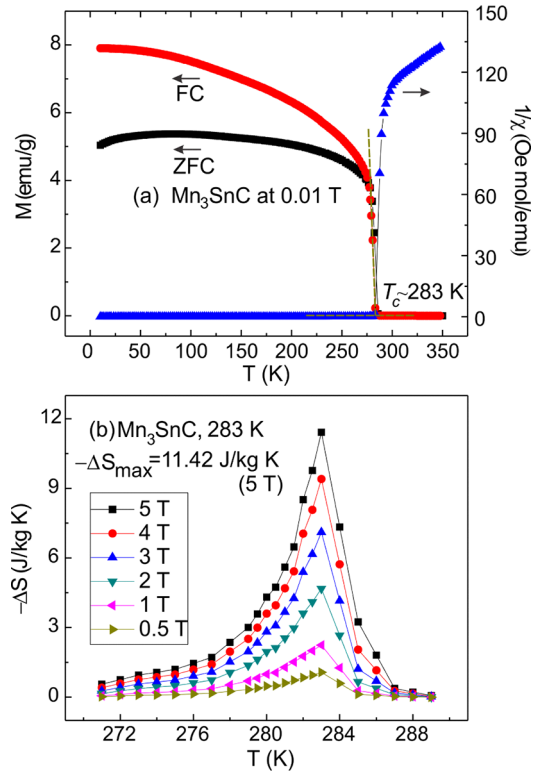

Figure 3. (a) Temperature dependence of the magnetization $\mathbf{M}(T)$ (FC, ZFC) at $\boldsymbol{H}$ = 0.01 T (left axis). The right axis shows the inverse susceptibility as a function of temperature. (b) Magnetic field-induced isothermal entropy change as a function of temperature for selected applied magnetic fields.

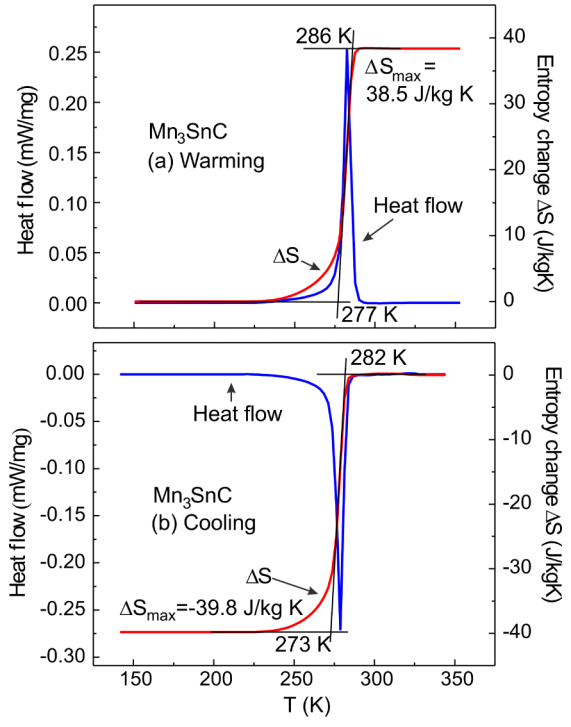

Figure 4. Temperature dependence of the heat flow (right axis) and entropy change (left axis) for Mn_3SnC. (a) Warming, with ΔS_{max} = 38.5 J/kg K (endothermic process). (b) Cooling, with ΔS_{max} = −39.8 J/kg K (exothermic process).

dx.doi.org/10.1021/ic403063t | Inorg. Chem. 2014, 53, 2317−2324

K. Figure 5 shows neutron diffraction patterns of Mn_3SnC at 260 K under 0, 0.5, and 6 T, respectively. Each diffraction

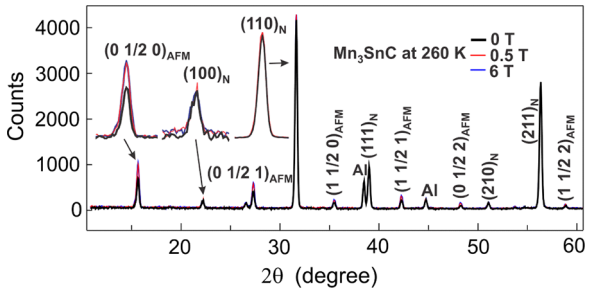

Figure 5. Neutron diffraction patterns of Mn_3SnC at 260 K under 0, 0.5, and 6 T, respectively. The antiferromagnetic peak $(0\ 1/2\ 0)_{AFM}$ and nuclear peaks $(100)_N$ and $(110)_N$ are magnified to show the variations of the magnetic and lattice under magnetic field.

pattern has been normalized to the zero field. The nuclear peaks of aluminum foil, which was used to wrap the sample, are also shown in Figure 5. All the aluminum nuclear peaks were unchanged under different magnetic field, as expected. As discussed above, the strongest ferromagnetic peak (1/2 1/2 0) overlaps the nuclear peak (100). With increasing magnetic field no significant change was found for this peak even under 6 T at 260 K, as shown in Figure 5. Hence no ferromagnetic component was obtained for the above experimental conditions. The refinement process further confirmed this result. However, the intensity of all the antiferromagnetic peaks under 0.5 T rose by about 45% as compared with the data under 0 T. For higher applied fields the intensity of AFM peaks changed very little up to 6 T. Identical results were obtained for a temperature of 277 K. Figure 6 shows the refinement results for the field dependence of the lattice parameter and magnetic

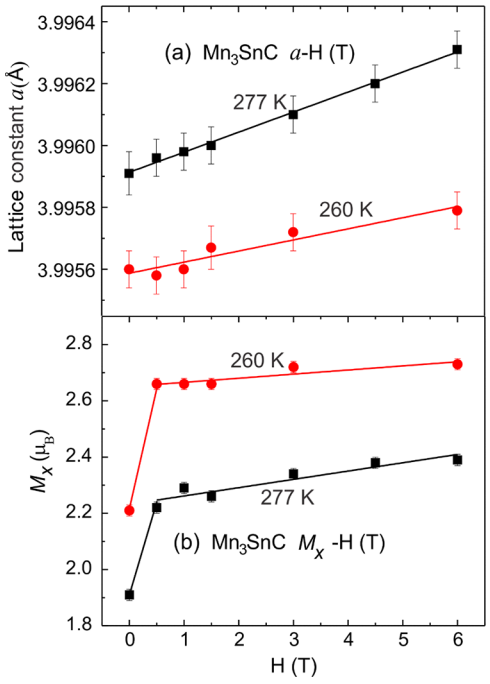

Figure 6. (a) Magnetic field dependence of the lattice parameter at 260 and 277 K. (b) Magnetic field dependence of the antiferromagnetic moment at 260 and 277 K.

moment for Mn_3SnC at 260 and 277 K. Both the antiferromagnetic moment and lattice parameter increase with increasing magnetic field. For the AFM moment, there is a sharp increase at a small field of 0.5 T, and then it slowly increases with further increase of field. The lattice parameter, on the other hand, increases linearly with increasing field. Figure 7a,b shows the isotherm magnetization curves $\mathbf{M}(H)$ of

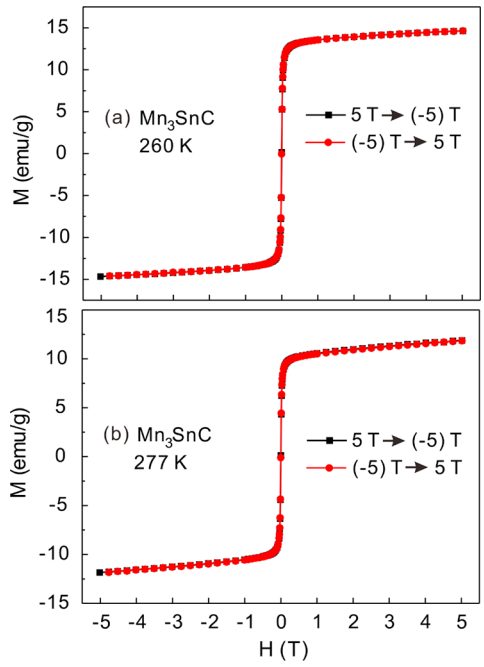

Figure 7. The isotherm magnetization curves $\mathbf{M}(H)$ of Mn_3SnC at (a) 260 K and (b) 277 K.

Mn_3SnC at 260 and 277 K, respectively. It can be seen from Figure 7 that the magnetization has a sharp change below 0.5 T, which corresponds with the neutron results. The maximum magnetization of Mn_3SnC is about $\mathbf{M}(H)$ = 15 emu/g (with 1 emu/g = 1 A m^2/kg), which corresponds to ~0.79 μ_B per molecule at 5 T in Figure 7. For the FM component in Mn_3SnC, it is difficult to confirm such tiny changes from NPD refinement. Since the magnetic field induces changes of both the antiferromagnetic moment and lattice parameter, it is important to confirm the relationship between the lattice and antiferromagnetic state in this class of material.

On the basis of previous studies on $Mn_{3-x}Cu_{0.5}Ge_{0.5}N$ and Mn_3Zn_xN,[25,26] the quantitative relationship between the lattice expansion and magnetic moment could lead to NTE behavior. Thus we investigate the variation of the antiferromagnetic moment and abnormal thermal expansion in Mn_3SnC. Figure 8 shows the temperature dependence of both the lattice parameter and magnetic moment of Mn_3SnC. As the crystal structure of Mn_3SnC maintains the cubic structure in the whole temperature range, the lattice parameter change is consistent with the volume change. Negative thermal expansion was observed in the temperature range of 275−290 K (ΔT = 15 K), with a linear thermal expansion coefficient $\alpha_l = \Delta L/L\Delta T$ of $\alpha_{l1} = -4.6 \times 10^{-5}$ K^{-1} in Mn_3SnC. The NTE effect occurs during the magnetic ordering transition process. The antiferromagnetic ordered moment begins to increase, while the lattice parameter jumps up at the transition. The ferromagnetic moment component on the z = 0 plane of $\mathbf{M}_1$ is 0.25(46) μ_B at 270 K, indicating that the value is too small to detect. At lower

dx.doi.org/10.1021/ic403063t | Inorg. Chem. 2014, 53, 2317−2324

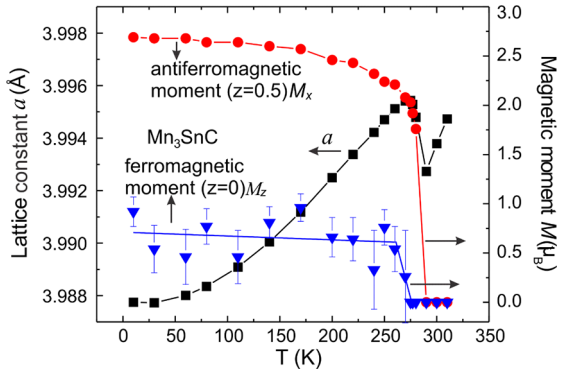

Figure 8. Temperature dependence of the lattice parameter (left axis) and ordered Mn moment in Mn_3SnC, including the antiferromagnetic moment on the z = 0.5 plane and the ferromagnetic moment on the z = 0 plane (right axis).

temperature the value remains below 1.0 μ_B. The ferromagnetic component on the z = 0.5 plane of $\mathbf{M_1}$ refines to 0.20(28) μ_B at 80 K, again within experimental uncertainty of zero. For this ferromagnetic component a nonzero value is observed below 80 K. In this instance, we deduce that the lattice is coupled with the antiferromagnetic component on the z = 0.5 plane of $\mathbf{M_1}$ in Mn_3SnC. To validate this conclusion, we tune the magnetic state and NTE behavior by doping and the introduction of vacancies in the Mn_3SnC lattice.

According to the NPD refinement results the crystal structures of $Mn_3Sn_{0.95}C_{0.9}$ and $Mn_3Sn_{0.93}Si_{0.07}C_{0.94}$ above the magnetic ordering temperature are the same as Mn_3SnC. The magnetic moments and lattice variation of them are different from that of Mn_3SnC below the magnetic ordering temperature (details will be discussed later). The lattice constants of $Mn_3Sn_{0.95}C_{0.9}$ and $Mn_3Sn_{0.93}Si_{0.07}C_{0.94}$ are 3.99083 Å and 3.99143 Å, respectively, at 300 K. Figure 9a shows the magnetic structure of $Mn_3Sn_{0.95}C_{0.9}$. We label this magnetic model $\mathbf{M_2}$, which differs from $\mathbf{M_1}$ (Figure 1b) in that there is not a ferromagnetic component on the z = 0.5 plane (Mn_3) and the spin direction of the Mn_1 is antiparallel to that of Mn_2. For $\mathbf{M_1}$, the magnetic structure is ferrimagnetic; for $\mathbf{M_2}$, the magnetic structure is purely antiferromagnetic.

Figure 9b shows the difference ($I_{obs} - I_{calc}$) of nuclear fitting only (black) for $Mn_3Sn_{0.95}C_{0.9}$ at 4 K, where the difference peaks between the top line and bottom line are magnetic peaks. For $Mn_3Sn_{0.95}C_{0.9}$, the magnetic reflections appear to be identical with Mn_3SnC in Figure 2c. However, if we use the magnetic model of Mn_3SnC to fit the magnetic peaks of $Mn_3Sn_{0.95}C_{0.9}$, the refinement process does not converge. It was found that the antiferromagntic components of $Mn_3Sn_{0.95}C_{0.9}$ can be indexed using the magnetic superlattice model of Mn_3SnC, so that the factor that leads to the failure in the refinement process is the ferromagnetic components. We therefore used this model setting the ferromagnetic components to zero (Figure 9a). The top solid line, in Figure 9b, shows the difference ($I_{obs} - I_{calc}$) of nuclear and magnetic fitting with model $\mathbf{M_2}$. The refinement converges rapidly and stably. All the magnetic peaks can be fit well without any ferromagnetic components. The antiferromagntic moments of $Mn_3Sn_{0.95}C_{0.9}$ are 2.36(4) μ_B on z = 0.5 plane and 1.4(1) μ_B on z = 0 plane at 4 K.

For $Mn_3Sn_{0.93}Si_{0.07}C_{0.94}$, the magnetic reflections correspond to the same propagation vector k = (1/2 1/2 0). If we consider the ferrimagnetic structure based on $\mathbf{M_1}$, the ferromagnetic

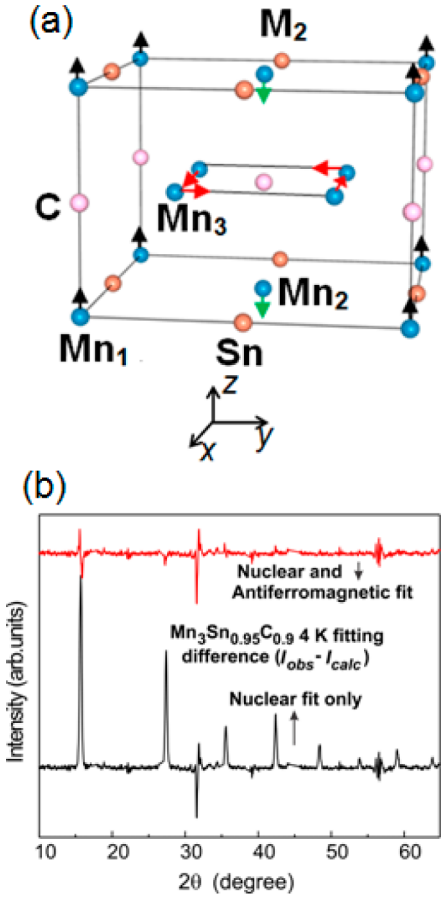

Figure 9. (a) Magnetic structure ($\sqrt{2}a$, $\sqrt{2}a$, a) of $Mn_3Sn_{0.95}C_{0.9}$, space group $P4$. We label this magnetic structure model $\mathbf{M_2}$. (b) ($I_{obs} - I_{calc}$) neutron powder diffraction pattern for $Mn_3Sn_{0.95}C_{0.9}$ at 4 K. (red) Nuclear and magnetic fits with magnetic model $\mathbf{M_2}$. (black) Nuclear fit only.

component intensity can be fit with various spin configurations. Both the ferrimagnetic structure and antiferromagnetic structure can be used to fit the neutron data, indicating that the (always small) ferromagnetic components are below our detection limit. Therefore we use the antiferromagnetic model in Figure 9a ($\mathbf{M_2}$) to estimate the antiferromagnetic component. The antiferromagntic moments of $Mn_3Sn_{0.93}Si_{0.07}C_{0.94}$ are 2.57(5) μ_B on z = 0.5 plane and 1.6(1) μ_B on z = 0 plane at 5 K.

Figure 10a,b shows the temperature dependence of the lattice parameter and magnetic moment for $Mn_3Sn_{0.95}C_{0.9}$ and $Mn_3Sn_{0.93}Si_{0.07}C_{0.94}$, respectively. Because of the cubic structure, variations of the lattice parameters with temperature have a similar correspondence to variations of the volumes in $Mn_3Sn_{0.95}C_{0.9}$ and $Mn_3Sn_{0.93}Si_{0.07}C_{0.94}$. We can see that the antiferromagnetic moment and NTE behavior are changed compared with that of Mn_3SnC. Then by comparing Figure 10 to Figure 8 we can reveal the relationship between the antiferromagnetic moment and lattice. In the NTE temperature range, the antiferromagnetic moment can be fit with a linear fitting method.

$$\mathbf{M}(T) = M_0 + \beta T \quad (2)$$

where M_0 is a constant and β is a scaling factor ($\beta = \Delta M/\Delta T$) that indicates the rate of change of the magnetic moment with temperature. For Mn_3SnC, the NTE range can be divided into

dx.doi.org/10.1021/ic403063t | Inorg. Chem. 2014, 53, 2317−2324

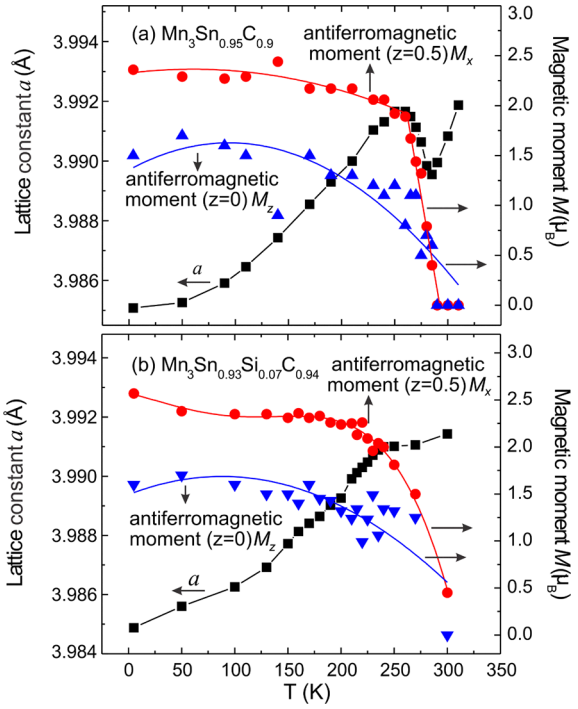

Figure 10. (a,b) Temperature dependence of the lattice parameter and ordered Mn moment in $Mn_3Sn_{1-\varepsilon}Si_\varepsilon C_{1-\delta}$ compounds. (a) $Mn_3Sn_{0.95}C_{0.9}$, antiferromagnetic moment on the z = 0.5 plane, z = 0 plane (right axis) and lattice parameter (left axis). (b) $Mn_3Sn_{0.93}Si_{0.07}C_{0.94}$, antiferromagnetic moment on the z = 0.5 plane, z = 0 plane (right axis) and lattice parameter (left axis).

two areas with different β values: $\beta_1' = \Delta M_1/\Delta T = -0.05\ \mu_B$/K in the range of 275−280 K, and the $\beta_1'' = \Delta M_1'/\Delta T \approx -\infty$ ($\arctan(\beta_1'') \approx -\pi/2$) in the range of 280−290 K. For the whole NTE range, we can use the average value β_1 between the β_1' and β_1'' to indicate the rate of change of the magnetic moment. We obtain the relation of $\beta_1' < \beta_1 < \beta_1''$.

For $Mn_3Sn_{0.95}C_{0.9}$, the linear thermal expansion coefficient α_{l2} of the NTE is -2.234×10^{-5} K^{-1} for the temperature range of 260−285 K (ΔT = 25 K). There are two antiferromagnetic components on the z = 0 and z = 0.5 planes of the $\mathbf{M_2}$ magnetic model, respectively. The variation of the antiferromagnetic moment on the z = 0.5 plane is consistent with that of the cubic lattice constant. The other antiferromagnetic component (z = 0 plane) is independent of the NTE behavior. Hence we use eq 2 to fit the variation of the AFM moment (z = 0.5 plane), yielding $\beta_2 = \Delta M_2/\Delta T = -0.05\ \mu_B$/K in the NTE range.

For $Mn_3Sn_{0.93}Si_{0.07}C_{0.94}$, Si substitution for Sn dramatically changes the thermal expansion properties of Mn_3SnC. $Mn_3Sn_{0.93}Si_{0.07}C_{0.94}$ exhibits nearly ZTE, with $\alpha_{l3} = 5.190 \times 10^{-7}$ K^{-1} for the temperature range of 240−270 K (ΔT = 30K). The variation of the antiferromagnetic moment on the z = 0 plane for the $\mathbf{M_2}$ magnetic model is similar to that of $Mn_3Sn_{0.95}C_{0.9}$ and is independent of the lattice variation. We use eq 2 to fit the AFM moment (z = 0.5 plane), the rate of change of the AFM moment with temperature $\beta_3 = \Delta M_3/\Delta T = -0.017\ \mu_B$/K in the temperature range of 240−270 K.

On the basis of the above discussion, we find a close relationship between the abnormal thermal expansion and the rate of change of the antiferromagnetic moment on the z = 0.5 plane: as to the variation of AFM moment, we obtained $-\beta_1 > -\beta_2 > -\beta_3$, while for the linear thermal expansion coefficients we found $-\alpha_{l1} > -\alpha_{l2} > -\alpha_{l3}$. This relationship reveals that the magnitude of the abnormal thermal expansion is controlled by the rate of change of the AFM moment. For all three samples, as $|\beta|$ gradually decreases, we realize nearly ZTE behavior in $Mn_3Sn_{0.93}Si_{0.07}C_{0.94}$. To clarify this transition, we can use the magnetic moment derivative dM/dT and the lattice constant derivative da/dT to display the discontinuous process. Figure 11 shows the result.

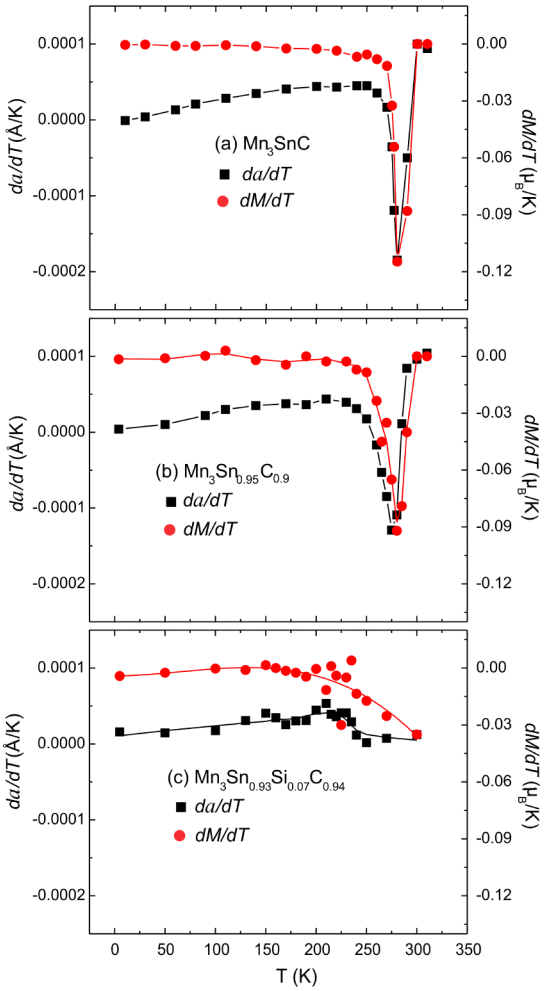

Figure 11. (a,b,c) Lattice parameter derivative (da/dT) and magnetic moment derivative (dM/dT) for the three samples. (a) Mn_3SnC. (b) $Mn_3Sn_{0.95}C_{0.9}$. (c) $Mn_3Sn_{0.93}Si_{0.07}C_{0.95}$.

For $Mn_3Sn_{1-\varepsilon}Si_\varepsilon C_{1-\delta}$, normal positive thermal expansion (PTE) is observed at low temperature. We can use the quadratic function to fit the PTE behavior.

$$a(T) = a_0T^2 + b_0T + C_0 \quad (3)$$

where $a(T)$ is lattice parameter at temperature T and a_0, b_0, and c_0 are constants. On the basis of eq 3, the rate of change of the lattice constant with respect to temperature can be described as:

$$da/dT = 2a_0T + b_0 \quad (4)$$

Note that da/dT is a linear function with respect to temperature T. If no magnetic field is applied, the slope $2a_0$ of the line is a constant. However, coupling between the magnetic order and the lattice will change, providing a strong correlation between da/dT and dM/dT. We can see that dM/

dx.doi.org/10.1021/ic403063t | Inorg. Chem. 2014, 53, 2317−2324

dT exhibits the same tendency as the da/dT function in Figure 11.

This result provides experimental evidence for the common assumption that the lattice is closely related to the magnetism in this class of compounds. We note that, in the range where the lattice and magnetic order are strongly coupled, the rates of change of the magnetic moment and the linear thermal expansion coefficient of $Mn_3Sn_{0.93}Si_{0.07}C_{0.94}$ are smaller than they are for the other two compounds. When the contribution of the magnetic order to the lattice expansion cancels that from the conventional anharmonic lattice vibration, we obtain ZTE behavior in $Mn_3Sn_{0.93}Si_{0.07}C_{0.94}$.

Vacancies and doping do not significantly change the magnetic structure in $Mn_3Sn_{1-\varepsilon}Si_\varepsilon C_{1-\delta}$ compounds, in contrast to the Mn_3Zn_xN[26] and $Mn_3Cu_{1-x}Ge_xN$[22−24] systems. The difference in behavior may be closely associated with the electronic states near the Fermi level. P. Tong et al.[31] studied the local structure of $Mn_3Cu_{1-x}Sn_xN$ via neutron diffraction and the neutron pair distribution function (PDF) technique. They pointed out that if the compounds have more p electrons (e.g., Sn, Ge), the strong p−d hybridization would stabilize the Γ^{5g} magnetic configuration,[31] and the Γ^{5g} magnetic structure has a close relationship with the NTE in these compounds. For the Γ^{5g} magnetic sturcture with propagation vector k = (0 0 0), there are no superlattice peaks, and the crystal and magnetic structures have the same primitive unit cell. However, the stable square antiferromagnetic structure shown in Figures 1b and 9a is a key factor to produce NTE/ZTE in $Mn_3Sn_{1-\varepsilon}Si_\varepsilon C_{1-\delta}$. For this magnetic structure with k = (1/2 1/2 0), there are superlattice magnetic peaks at low temperature and the magnetic unit cell is a superlattice cell. With this structure, the rate of change of the magnetic moment controls the NTE/ZTE, and vacancies and doping adjust the variation of the magnetic moment. We can thereby control the NTE/ZTE by introducing vacancies and/or doping in $Mn_3Sn_{1-\varepsilon}Si_\varepsilon C_{1-\delta}$. The NTE behavior is related to the lattice entropy in Mn_3SnC, and we can tune the lattice entropy by introducing vacancies and doping in $Mn_3Sn_{1-\varepsilon}Si_\varepsilon C_{1-\delta}$. In addition, magnetic field also can change the antiferromagnetic moment and lattice parameter in Mn_3SnC, which means we might be able to control the lattice entropy by magnetic field. These results provide a possibility to extract the lattice entropy in this class of materials.

CONCLUSIONS

In summary, the NTE effect in this system is related to a commensurate (square) AFM state, and we have obtained a quantitative relationship between the rate of change of the AFM moment ($\beta = \Delta M/\Delta T$) and the linear thermal expansion coefficient ($\alpha_l = \Delta L/L\Delta T$) to produce NTE/ZTE in $Mn_3Sn_{1-\varepsilon}Si_\varepsilon C_{1-\delta}$. The magnetic entropy only accounts for ∼29% of the total entropy associated with the magnetic/structural phase transition in Mn_3SnC. The lattice entropy is related to the NTE, which can be tuned by magnetic field. The research presented here provides further clues to not only design zero thermal expansion materials but also to control the lattice entropy in this class of materials.

AUTHOR INFORMATION

Corresponding Author

*E-mail: congwang@buaa.edu.cn (C.W.), qing.huang@nist.gov (Q.H.).

Notes

The authors declare no competing financial interest.

ACKNOWLEDGMENTS

This work is financially supported by National Natural Science Foundation of China (NSFC) (No. 91122026 and No. 51172012), the Ph.D. Programs Foundation of Ministry of Education of China (No. 20111102110026), and China Scholarship Council.

REFERENCES

(1) He, T.; Huang, Q.; Ramirez, A. P.; Wang, Y.; Regan, K. A.; Rogado, N.; Hayward, M. A.; Haas, M. K.; Slusky, J. S.; Inumara, K.; Zandbergen, H. W.; Ong, N. P.; Cava, R. J. *Nature* **2001**, *411*, 54−56.
(2) Uehara, M.; Yamazaki, T.; Kôri, T.; Kashida, T.; Kimishima, Y.; Hase, I. *J. Phys. Soc. Jpn.* **2007**, *76*, 034714−1−5.
(3) Kamishima, K.; Goto, T.; Nakagawa, H.; Miura, N.; Ohashi, M.; Mori, N.; Sasaki, T.; Kanomata, T. *Phys. Rev. B* **2000**, *63*, 024426−1−6.
(4) Wen, Y. C.; Wang, C.; Sun, Y.; Nie, M.; Chu, L. H. *J. Magn. Magn. Mater.* **2010**, *322* (20), 3106−3108.
(5) Asano, K.; Koyama, K.; Takenaka, K. *Appl. Phys. Lett.* **2008**, *92*, 161909−1−3.
(6) Chi, E. O.; Kim, W. S.; Hur, N. H. *Solid State Commun.* **2001**, *120*, 307−310.
(7) Sun, Y.; Wang, C.; Chu, L. H.; Wen, Y. C.; Nie, M.; Liu, F. S. *Scr. Mater.* **2010**, *62* (9), 686−689.
(8) Ding, L.; Wang, C.; Chu, L. H.; Yan, J.; Na, Y. Y.; Huang, Q. Z.; Chen, X. L. *Appl. Phys. Lett.* **2011**, *99*, 251905−1−4.
(9) Takenaka, K.; Ozawa, A.; Shibayama, T.; Kaneko, N.; Oe, T.; Urano, C. *Appl. Phys. Lett.* **2011**, *98*, 022103−1−3.
(10) Chu, L. H.; Wang, C.; Yan, J.; Na, Y. Y.; Ding, L.; Sun, Y.; Wen, Y. C. *Scr. Mater.* **2012**, *67*, 173−176.
(11) Takenaka, K.; Takagi, H. *Appl. Phys. Lett.* **2005**, *87*, 261902−1−3.
(12) Huang, R. J.; Li, L. F.; Cai, F. S.; Xu, X. D.; Qian, L. H. *Appl. Phys. Lett.* **2008**, *93*, 081902−1−3.
(13) Sun, Y.; Wang, C.; Wen, Y. C.; Zhu, K. G.; Zhao, J. T. *Appl. Phys. Lett.* **2007**, *91*, 231913−1−3.
(14) Chen, J.; Nittala, K.; Forrester, J. S.; Jones, J. L.; Deng, J. X.; Yu, R. B.; Xing, X. R. *J. Am. Chem. Soc.* **2011**, *133*, 11114−11117.
(15) Huang, R. J.; Liu, Y. Y.; Fan, W.; Tan, J.; Xiao, F. R.; Qian, L. H.; Li, L. F. *J. Am. Chem. Soc.* **2013**, *135*, 11469−11472.
(16) Tohei, T.; Wada, H.; Kanomata, T. *J. Appl. Phys.* **2003**, *94*, 1800−1802.
(17) Yu, M. H.; Lewis, L. H.; Moodenbaugh, A. R. *J. Appl. Phys.* **2003**, *93*, 10128−10130.
(18) Kaneko, T.; Kanomata, T.; Miura, S.; Kido, G.; Nakagawa, Y. *J. Magn. Magn. Mater.* **1987**, *70*, 261−262.
(19) Kanomata, T.; Kikuchi, M.; Kaneko, T.; Kamishima, K.; Bartashevich, M. I.; Katori, H. A.; Goto, T. *Solid State Commun.* **1997**, *101* (11), 811−814.
(20) Wang, B. S.; Tong, P.; Sun, Y. P.; Lou, X.; Zhu, X. B.; Li, G.; Zhu, X. D.; Zhang, S. B.; Yang, Z. R.; Song, W. H.; Dai, J. M. *Europhys. Lett.* **2009**, *85*, 47004−1−5.
(21) Fruchart, D.; Bertaut, E. F. *J. Phys. Soc. Jpn.* **1978**, *44*, 781−791.
(22) Iikubo, S.; Kodama, K.; Takenaka, K.; Takagi, H.; Takigawa, M.; Shamoto, S. *Phys. Rev. Lett.* **2008**, *101*, 205901−1−4.
(23) Iikubo, S.; Kodama, K.; Takenaka, K.; Takagi, H.; Shamoto, S. *Phys. Rev. B.* **2008**, *77*, 020409−1−4.
(24) Kodama, K.; Iikubo, S.; Takenaka, K.; Takigawa, M.; Takagi, H.; Shamoto, S. *Phys. Rev. B.* **2010**, *81*, 224419−1−8.
(25) Song, X.; Sun, Z.; Huang, Q. Z.; Rettenmayr, M.; Liu, X.; Seyring, M.; Li, G.; Rao, G.; Yin, F. *Adv. Mater.* **2011**, *23* (40), 02552−1−5.
(26) Wang, C.; Chu, L. H.; Yao, Q. R.; Sun, Y.; Wu, M. M.; Ding, L.; Yan, J.; Na, Y. Y.; Tang, W. H.; Li, G. N.; Huang, Q. Z.; Lynn, J. W. *Phys. Rev. B.* **2012**, *85*, 220103−1−5.

(27) Wen, Y. C.; Wang, C.; Nie, M.; Sun, Y.; Chu, L. H.; Dong, C. *Appl. Phys. Lett.* **2010**, *96*, 041903−1−3.
(28) Wen, Y. C.; Wang, C.; Sun, Y.; Nie, M.; Fang, L.; Tian, Y. J. *Solid State Commun.* **2009**, *149* (37−38), 1519−1522.
(29) Larson, A. C.; Von Dreele, R. B. *General Structure Analysis System (GSAS)*, Technical Report LAUR 86−748 for Los Alamos National Laboratory: Los Alamos, NM, 2004.
(30) Phan, M. H.; Yu, S. C. *J. Magn. Magn. Mater.* **2007**, *308*, 325−340.
(31) Tong, P.; Louca, D.; King, G.; Llobet, A.; Lin, J. C.; Sun, Y. P. *Appl. Phys. Lett.* **2013**, *102*, 041908−1−4.